


An indoor DSO-based ceiling-vision odometry system for indoor industrial environments

Abdelhak Bougouffa^{1,2,†,*} , Emmanuel Seigneze¹, Samir Bouaziz¹ and Florian Gardes²

¹ Université Paris-Saclay, ENS Paris-Saclay, CNRS, SATIE, 91190, Gif-sur-Yvette, France.;
firstname.lastname@universite-paris-saclay.fr

² ez-Wheel - IDEC Corp., 16400, La Couronne, France; f.gardes@ez-wheel.com

* Correspondence: abdelhak.bougouffa@gmail.com

† This paper is an extended version of our paper published in 2022 17th International Conference on Control, Automation, Robotics and Vision (ICARCV) [1].

‡ Current address: Astek Technology, 92100, Boulogne-Billancourt, France.

Abstract: Autonomous Mobile Robots operating in indoor industrial environments require a localization system that is reliable and robust. While Visual Odometry (VO) can offer a reasonable estimation of the robot's state, traditional VO methods encounter challenges when confronted with dynamic objects in the scene. Alternatively, an upward-facing camera can be utilized to track the robot's movement relative to the ceiling, which represents a static and consistent space. We introduce in this paper Ceiling-DSO, a ceiling-vision system based on Direct Sparse Odometry (DSO). Unlike other ceiling-vision systems, Ceiling-DSO takes advantage of the versatile formulation of DSO, avoiding assumptions about observable shapes or landmarks on the ceiling. This approach ensures the method's applicability to various ceiling types. Since no publicly available dataset for ceiling-vision exists, we created a custom dataset in a real-world scenario and employed it to evaluate our approach. By adjusting DSO parameters, we identified the optimal fit for online pose estimation, resulting in acceptable error rates compared to ground truth. We provide in this paper a qualitative and quantitative analysis of the obtained results.

Keywords: State estimation; mobile robotics; indoor; visual odometry; ceiling-vision; dynamic environment; industrial environment; DSO; Ceiling-DSO.

1. Introduction

State estimation remains an open research problem in the field of mobile robotics. The ability of a mobile robot to accomplish autonomous mobility tasks depends on its knowledge of its position and orientation, referred to as its pose, in space.

In indoor industrial environments, mobile robots are commonly classified into two main categories: *Automated Guided Vehicles (AGVs)* and *Autonomous Mobile Robots (AMRs)*. In one hand, AGVs rely on a dedicated infrastructure for navigation. One approach is *active guiding* [2], where, for example, wires are embedded under the ground's surface to transmit wireless signals that the robot detects and follows. Alternatively, *passive guidance* methods [3,4] can be employed, involving magnetic tapes, RFID tags, or visual lanes.

On the other hand, AMRs require little or no prior knowledge about the environment. These robots rely on their sensors to perceive and comprehend the surrounding environment, allowing them to estimate their ego-motion and navigate. Over the past decade, there has been a significant interest in developing AMRs. Their flexibility and ease of commissioning make them highly suitable for various industrial applications.

In indoor robotics, several sensors can be used for estimating a robot's pose. One commonly used method consists of utilizing wheel encoders to incrementally estimate the robot's motion, which we call *odometry*. However, the mechanical coupling, the wheel slippage, and the absence of external correction make the odometry unreliable for long-term usage [5] due to the drift caused by accumulating errors over time.

Alternatively, cameras can be employed to calculate the incremental changes in a moving robot's position and orientation, a technique commonly referred to as *Visual*

Published: December 5, 2024



Copyright: © 2024 by the authors.
This pre-print article is shared under the Creative Commons Attribution (CC BY) license (<https://creativecommons.org/licenses/by/4.0/>).

Odometry (VO) [6]. The term “*visual odometry*” was first introduced by Nister et al. [7], it involves incrementally estimating camera motion from a perceived stream of images.

From a conceptual standpoint, Visual Odometry approaches can be categorized into two main families: *indirect (feature-based) methods* [8–11] and *direct methods* [12,13]. Indirect methods necessitate a preprocessing step that involves extracting a set of *features* using *feature detection* techniques. These features are then used to minimize *geometric error*. On the other hand, direct methods use the *raw pixel intensity values* to minimize *photometric error*, eliminating the need for explicit feature extraction. Another classification criterion for VO approaches is the density of their estimated 3D geometries. VO can estimate a *dense* 3D geometry [14], a *sparse* one [8,10], or a *semi-dense* geometry [15].

Visual Odometry (VO) and *Visual Simultaneous Localization and Mapping (vSLAM)* differ in their map management strategy. VO focuses only on maintaining consistency in a partial local map and utilizes it to incrementally estimate robot motion. In contrast, vSLAM algorithms aim to provide, alongside the estimated poses, a globally consistent map, incorporating corrections on loop closing [6].

In the context of our mobile industrial robot, which operates in a highly dynamic environment with multiple robots and humans sharing the same space, the VO estimation can be challenging. Indeed, the presence of moving objects in the scene necessitates their detection and exclusion while calculating the robot’s ego-motion [16,17]. This task tends to be complicated and resource-intensive.

To address the challenges posed by indoor dynamic environments, a viable solution involves using an upward-facing camera to monitor ceiling patterns and track the movements of the robot. Wooyeon et al. were the first to propose such an approach [18]. They employed a monocular upward-facing camera along with the Harris corner detector to extract corner features from the captured images. These corners serve as landmarks within an SLAM framework based on the *Extended Kalman Filter (EKF)*. This method incorporates a multi-view representation of the landmarks to improve data association and enhance the accuracy of the system.

Ceiling vision-based odometry and SLAM approaches often rely on making assumptions about the specific shapes and patterns observable on the ceiling. Kim et al. [19] have taken advantage of this by exploiting known ceiling landmark classes (circular landmarks representing objects like *lamps, speakers, fire alarms, etc.*). This valuable information is used in a FastSLAM framework to effectively track the robot’s pose and construct the map.

Another research effort by Hwang and Song [20] used a similar approach, where their system detects three distinct types of landmarks: *corners, circular lamps, and doors*. Corner features are extracted using the *Features from Accelerated Segment Test (FAST)* detector. The lamps are identified by locating the brightest patches in the ceiling image by using a *Canny* edge detector and performing geometric circle fitting on the bright zone. Doors are recognized by detecting two vertical lines intersected by a horizontal line. These detected features are then integrated into an EKF-SLAM framework, making use of the robot’s odometry during the prediction step.

Alternative methods involve making assumptions about the boundaries of the ceiling. Choi et al. [21,22] proposed an approach using an EKF-SLAM framework with a monocular camera. They used the boundaries between the ceiling and the walls, represented as lines with intersection constraints, to construct a features map. The authors took advantage of the fact that, in their test environment, ceiling regions dominate most of the images captured from the ceiling-view camera, while walls occupy the remaining portions.

Similarly, other approaches adopt the same assumption and focus on extracting the ceiling boundaries, which are then compared to a known building blueprint using a *Monte Carlo Localization (MCL)* approach while employing an observation model based on *Ceiling Space Density (CSD)* [23].

In other methods, distinct visual tags are carefully placed on the ceiling to simplify the localization process. Li et al. [24] designed artificial markers that are easily detectable and placed them on the ceiling. By processing the images captured from the ceiling camera,

these markers are detected, identified, and used to determine the camera’s position and orientation with respect to them. The obtained information is then incorporated in a graph-based optimization algorithm, implemented within a Bayesian estimation framework.

However, all the assumptions discussed above often do not hold in open warehouses or industrial spaces. The vast working spaces may be too wide to capture both the ceiling and the walls in a single image. Moreover, ceilings in such environments tend to be high and may consist of inclined surfaces or be distributed across different height levels. To address these challenges, we propose employing a generic visual odometry approach using a ceiling-vision camera. Specifically, we have chosen to make use of the *Direct Sparse Odometry (DSO)*. Being a direct approach, DSO allows us to track the camera’s movement even in regions with limited distinct features. Our objective is to propose and evaluate a generic framework for ceiling observation that minimizes assumptions about the observable shapes or landmarks on the ceiling.

In this paper, which extends our previous work [1], we present and evaluate Ceiling-DSO, a ceiling-vision odometry system based on *Direct Sparse Odometry (DSO)*. Our experiments were conducted in a real-world environment using a modular industrial mobile robot platform. We systematically varied the DSO parameters and carefully examined their impact on the system’s performance and the quality of the estimated trajectories. To evaluate the estimated trajectories, we compared them with those obtained from a LiDAR-based SLAM solution, used as ground truth. Furthermore, we offer both qualitative and quantitative analyses of the obtained results.

The rest of this paper is structured as follows: Section 2 introduces the original formulation of DSO and outlines the assumptions made in implementing Ceiling-DSO. In section 3, we provide details about the experiment setup, including the robot’s sensors, the dataset generated for validation purposes, and the methodology employed in conducting the experiments. The results of our study are presented and discussed in section 4. Finally, section 5 summarizes the conclusions of this work and discusses potential future directions.

2. Ceiling Direct Sparse Odometry

The *Direct Sparse Odometry (DSO)*, introduced by Engel et al. [12], is a monocular visual odometry method that falls under the category of direct methods. Unlike feature-based visual odometry approaches that rely on a limited set of features for motion estimation, direct methods use information from all pixels in the image. Direct methods can be further classified into three categories based on the density of the generated point cloud: *dense*, *semi-dense* and *sparse*.

Dense methods leverage all pixels in the image to generate a high-density point cloud. However, this typically leads to computationally intensive algorithms due to the large amount of data being processed.

Semi-dense methods aim to reduce the number of processed by selecting a subset of points for processing. These methods strike a balance between accuracy and computational efficiency.

Sparse methods only consider a small subset of points for processing. This approach further reduces the computational load but may sacrifice some level of detail in the generated point cloud.

These different categories of direct methods offer varying trade-offs between accuracy and computational complexity, allowing researchers to choose an approach that best suits their specific requirements.

DSO belongs to the third category, it employs a gradient-based approach and uniformly select candidate points from regions with high contrast. By strategically choosing these points, DSO aims to enhance the estimation of camera motion and achieve accurate odometry while keeping the amount of processed data suitable for real-time applications. A *photometric error minimization* process is performed on these selected candidate points.

In the context of direct visual odometry/SLAM, the use of a *global shutter* camera is preferable for capturing frames simultaneously. This type of camera ensures that all

pixels of an image are acquired at the same instant. On the other hand, *rolling shutter* cameras capture image pixels sequentially, which can introduce a systematic drift in the state estimation, making these type of cameras unsuitable for DSO. However, this effect can be accounted for in the optimization process by measuring and compensating it. For instance, Schubert et al. [25] introduced a DSO-based approach that incorporates the rolling shutter constraint and estimates the capture time, thereby improving trajectory estimation when using a rolling-shutter camera.

In this work, we adopt the same formulation as the original DSO [12]. We model the camera sensor as a pinhole camera and utilize the intrinsic matrix \mathbf{K} for geometric projection. This projection maps 3D points onto the image plane Ω and is denoted as $\Pi_{\mathbf{K}}$. Additionally, we use the back-projection function $\Pi_{\mathbf{K}}^{-1}$ to convert a 2D point in the image plane along with its depth information into the corresponding 3D world coordinates.

$$\text{with: } \begin{cases} \mathbf{K} \in \mathbb{R}^{3 \times 3} & \text{Cameras intrinsic matrix} \\ \Omega \in \mathbb{R}^{2 \times 2} & \text{Image plane} \\ \Pi_{\mathbf{K}} : \mathbb{R}^3 \rightarrow \Omega & \text{Projection onto the image plane } \Omega \\ \Pi_{\mathbf{K}}^{-1} : \Omega \rightarrow \mathbb{R}^3 & \text{Back-projection from } \Omega \text{ to the 3D world} \end{cases}$$

In line with DSO, we consider *photometric calibration* [26]. For each frame “ i ”, the camera observes the raw intensity I_i^{RAW} of a pixel x . This intensity is defined as a function of various factors, including irradiance B_i , exposure time t_i , a non-linear response function $G : \mathbb{R} \rightarrow [0, 255]$, and lens attenuation (vignetting) $V : \Omega \rightarrow [0, 1]$.

$$I_i^{RAW}(x) = G(t_i V(x) B(x)) \quad (1)$$

$$\text{with: } \begin{cases} i \in \mathbb{N} & \text{A number to index frames} \\ x \in \Omega & \text{A pixel on the image plane } \Omega \\ t_i \in \mathbb{R} & \text{Exposure time of the frame } i \\ I_i^{RAW} : \Omega \rightarrow [0, 255] & \text{Raw pixel intensities image} \\ I_i : \Omega \rightarrow [0, 255] & \text{Photometrically corrected image} \\ G : \mathbb{R} \rightarrow [0, 255] & \text{Non-linear response function} \\ V : \Omega \rightarrow [0, 1] & \text{Lens attenuation} \\ B_i : \Omega \rightarrow [0, 1] & \text{Irradiance} \end{cases}$$

By reverting the non-linear function and compensating for the vignetting effect on the image, we can calculate the photometrically corrected image I_i as shown in equation (2), which is derived from equation (1).

$$I_i(x) \triangleq t_i B_i(x) = \frac{G^{-1}(I_i^{RAW}(x))}{V(x)} \quad (2)$$

The overall photometric error across all frames can be expressed as follows:

$$E_{\text{photometric}} = \sum_{i \in N} \sum_{\mathbf{p} \in P_i} \sum_{j \in \text{obs}(\mathbf{p})} E_{i, \mathbf{p}, j} \quad (3)$$

Considering a total of N frames, let P_i denote the set of points observed in the i -th frame. The variable j iterates over $\text{obs}(\mathbf{p})$, representing all frames in which the point \mathbf{p} is visible. The partial photometric error term $E_{i, \mathbf{p}, j}$ is defined as a weighted sum of Huber [27] norms, calculated within a neighborhood pattern of points surrounding the point \mathbf{p} , denoted by set $\mathcal{N}_{\mathbf{p}}$.

$$E_{i, \mathbf{p}, j} = \sum_{\mathbf{p}' \in \mathcal{N}_{\mathbf{p}}} w_{\mathbf{p}'} \left\| (I_j[\mathbf{p}'] - b_j) - \frac{t_j e^{a_j}}{t_i e^{a_i}} (I_i[\mathbf{p}] - b_i) \right\|_{\gamma} \quad (4)$$

$$\text{with Huber's norm } \|\alpha\|_\gamma \triangleq \begin{cases} \frac{1}{2}\alpha^2 & \text{for } |\alpha| < \gamma \\ \gamma \cdot (|\alpha| - \frac{1}{2}\gamma) & \text{otherwise} \end{cases}$$

$$\text{and } w_{\mathbf{p}} \triangleq \frac{c^2}{c^2 + \|\nabla I_i(\mathbf{p})\|_2^2} \text{ with } c \in \mathbb{R}$$

The Huber norm is a hybrid norm, combining the ℓ_1 and ℓ_2 norms and offering robustness against outliers while being differentiable throughout. As a result, it serves as a well-suited error measurement for gradient-based optimization.

The residual term within the summation (4) accounts for the discrepancy between the intensity values of point \mathbf{p} in the current frame (i) and its intensity across all frames where it is observable $j \in \text{obs}(\mathbf{p})$. To account for the unknown exposure times, the intensity is modeled as an affine brightness transfer function [26]. The \mathbf{p}' in equation (4) represents the projection of point \mathbf{p} , which is seen in the frame (i), onto the frame (j) with an estimated depth of $d_{\mathbf{p}}$. The projection matrix relies on the partial camera motion transform $\Delta\mathbf{T}_{j,i}$, which describes the transformation between camera poses \mathbf{T}_i and \mathbf{T}_j .

$$\mathbf{p}' = \Pi_{\mathbf{K}}(\mathbf{R}\Pi_{\mathbf{K}}^{-1}(\mathbf{p}, d_{\mathbf{p}}) + \mathbf{t}) \quad (5)$$

$$\text{with: } \Delta\mathbf{T}_{j,i} = \begin{bmatrix} \mathbf{R} & \mathbf{t} \\ 0 & 1 \end{bmatrix} = \mathbf{T}_j\mathbf{T}_i^{-1}$$

The minimization of the error term of equation (4) is achieved using a Gauss-Newton optimization algorithm, which iterates through 6 steps. This optimization is performed on the Lie algebra $\mathfrak{se}(3)$, where the left- \oplus operator is defined as follows:

$$\oplus : \mathfrak{se}(3) \times \text{SE}(3) \rightarrow \text{SE}(3) \quad (6)$$

$$\text{with: } \begin{cases} \mathbf{x}_i \in \mathfrak{se}(3), & \mathbf{T}_i \in \text{SE}(3) \\ \mathbf{x}_i \oplus \mathbf{T}_i \triangleq e^{\mathbf{x}_i} \cdot \mathbf{T}_i \end{cases}$$

For more details about Lie groups in the context of robotics and state estimation, readers are encouraged to refer to the paper by Solà et al. [28]. This work delves into the applications of the Lie groups theory in robotics and state estimation, providing valuable insights for researchers in the field.

In the optimization process, the parameters to be optimized are denoted as $\zeta \in \text{SE}(3)^n \times \mathbb{R}^m$. These parameters encompass both geometric aspects, such as poses, inverse depth values, and camera intrinsics, as well as photometric parameters, represented by the affine brightness parameters (a_i, b_i) . Within the rigid motion manifold $\text{SE}(3)$, we have an initial evaluation point denoted as ζ_0 , and the accumulated delta updates are represented by $\mathbf{x} \in \mathfrak{se}(3)^n \times \mathbb{R}^m$. The current state estimate can be obtained by $\zeta = \mathbf{x} \oplus \zeta_0$, using the left- \oplus operator, which is extended beyond $\text{SE}(3)$ elements as a regular addition.

This optimization process of the photometric error (3) is formulated as a Gauss-Newton system, which is defined as follows:

$$\mathbf{H} = \mathbf{J}^T \mathbf{W} \mathbf{J} \quad (7)$$

$$\mathbf{b} = -\mathbf{J}^T \mathbf{W} \mathbf{r} \quad (8)$$

In the equations above, the vector $\mathbf{r} \in \mathbb{R}^n$ represents the collection of residuals, $\mathbf{W} \in \mathbb{R}^{n \times n}$ is a square diagonal matrix with each diagonal element representing a weight factor, and $\mathbf{J} \in \mathbb{R}^{n \times d}$ is the Jacobian matrix of the residuals vector \mathbf{r} .

Consider r_k as an individual residual from the vector \mathbf{r} , and let J_k represent its corresponding row in the Jacobian matrix \mathbf{J} . The residual r_k contains: the camera poses at frames “ i ” and “ j ”, denoted respectively, \mathbf{T}_i and \mathbf{T}_j ; the inverse depth d_p , the camera intrinsics \mathbf{K} , and the affine brightness parameters a_i, a_j, b_i and b_j .

$$\text{with: } (\mathbf{T}_i, \mathbf{T}_j, d_p, a_i, a_j, b_i, b_j) = \mathbf{x} \oplus \zeta_0 \quad (9)$$

$$r_k = (I_j[\mathbf{p}'(\mathbf{T}_i, \mathbf{T}_j, d, \mathbf{K})] - b_j) - \frac{t_j e^{a_j}}{t_i e^{a_i}} (I_i - b_i) \quad (10)$$

$$\mathbf{J}_k = \frac{\partial r_k((\delta + \mathbf{x}) \oplus \zeta_0)}{\partial \delta} \quad (11)$$

During the Gauss-Newton optimization process in DSO, a sliding window of N_f keyframes is employed. Any points that fall outside this window are marginalized, meaning they are no longer actively considered in the optimization, which helps keeping the execution time bounded.

In our Ceiling-DSO implementation, we simplified the DSO formulation by assuming a linear response function $G(\mathbf{x})$. Additionally, we used lenses without vignetting, so:

$$\begin{cases} \forall \mathbf{x} \in \Omega : G(\mathbf{x}) = \mathbf{x} \\ \forall \mathbf{x} \in \Omega : V(\mathbf{x}) = 1 \end{cases} \quad (12)$$

3. Experiment

3.1. Experimental platform

In our experiments, we employed a mobile industrial robot prototype (figure 1). This platform is a modular, differential-drive robot that utilizes two self-contained motorized wheels powered by the *ez-Wheel Safety Wheel Drive (SWD™)* technology. This prototype represents an evolution of our previously validated SmartTrolley platform [29]. Its primary objective is to facilitate the movement of heavy loads indoors, particularly in industrial environments. We carefully designed and sized the robot to handle a maximum load capacity of 2 tonnes (2000kg), however, in this experiment, we used a plexiglass structure to facilitate moving the robot during the test phase. To prioritize safety, the robot is programmed to operate solely at low speeds of approximately $5\text{km} \cdot \text{h}^{-1}$ ($1.4\text{m} \cdot \text{s}^{-1}$).



Figure 1. The SWD Starter Kit

The robot is equipped with a pair of incremental wheels encoders, two cameras, the first is an *Intel® RealSense™ D435i* facing forward, while the second is an *Intel® RealSense™ 455* facing upward. Furthermore, the robot integrates an *IDEAL S2L* safety LiDAR, covering a maximal range of 30m.

The platform is equipped with a powerful embedded industrial computer, specifically the *Neosys Nuvo-7002LP*, featuring an 8th Generation *Intel® Coffee lake Core™ i5* processor

and 16GB DDR4 2666/2400 SDRAM. The computer operates on the *Ubuntu 20.04* operating system, complemented by the robotics middleware *ROS Noetic*. This used this embedded computer to run the differential-drive kinematic model for robot control and for gathering raw sensor data. To enable teleoperation, we equipped the computer with a wireless transceiver and used a wireless joystick to control the robot remotely.

The platform leverages the safety LiDAR’s low-level obstacle detection capabilities. We established two distinct detection zones for enhanced safety measures. The first zone, referred to as the *Safety-Limited Speed (SLS)* zone, is activated when the robot approaches an obstacle, allowing for reduced speed. The second zone, known as the *Safe Direction Indication (SDI)* zone, is smaller and prevents the robot from moving towards nearby obstacles. These detection and response behaviors have been implemented at the lowest level of the system (in the wheels’ microcontrollers). To facilitate robust and secure integration, the LiDAR transmits the SDI and SLS signals directly to the motorized wheels via secure *Output Signal Switching Device (OSSD)* outputs.

3.2. Dataset

Our experiment took place within a spacious indoor open area measuring $21 \times 15\text{m}$. Throughout the experiment, we gathered raw sensor data from various sources, including odometry readings, stereo up-facing camera images, forward-facing camera images, and LiDAR range measurements.

In our test environment, the ceiling is inclined (triangular structure), with varying heights between 4 and 6 meters. The ceiling’s characteristics, such as shapes and landmarks, may differ across different regions of the test area. For reference, figure 2 provides example images captured by the up-facing camera, showcasing the visual appearance of the ceiling in our experimental setup.

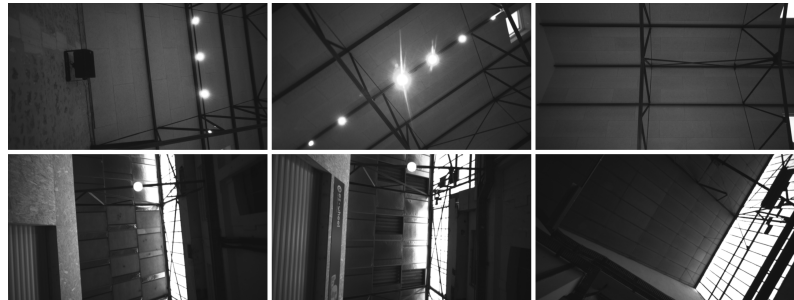


Figure 2. Sample images obtained from the up-facing camera offer a visual appearance of the test environment’s ceiling.

3.3. Methodology

To assess the performance of the Ceiling-DSO, we conducted an evaluation using a series of sequences from our collected dataset. Our analysis focused on investigating the impact of different factors, namely the *size of input images*, the *frame rate*, and the *maximum size of the optimization window*. We aimed to determine how these parameters affect both the execution time and the quality of the estimated trajectory. By identifying favorable parameter combinations through this evaluation, our objective was to optimize the Ceiling-DSO for real-time applications.

Utilizing the data obtained from the LiDAR, we computed a ground truth trajectory by employing the open-source LaMa SLAM algorithm [30]. The resulting map of the test environment, generated through this SLAM algorithm, is visually depicted in figure 3.

We carried out our experiment on a planar surface, utilizing a camera and a 2D LiDAR that were fixed on the robot. We refer to the ground truth 2D trajectory in 2D as \mathcal{G} . As DSO utilizes a monocular camera, its estimated trajectory, denoted as \mathcal{P} , is only valid up to a scale factor $\lambda \in \mathbb{R}^+$. While the DSO trajectory is 3-dimensional, the ground truth trajectory

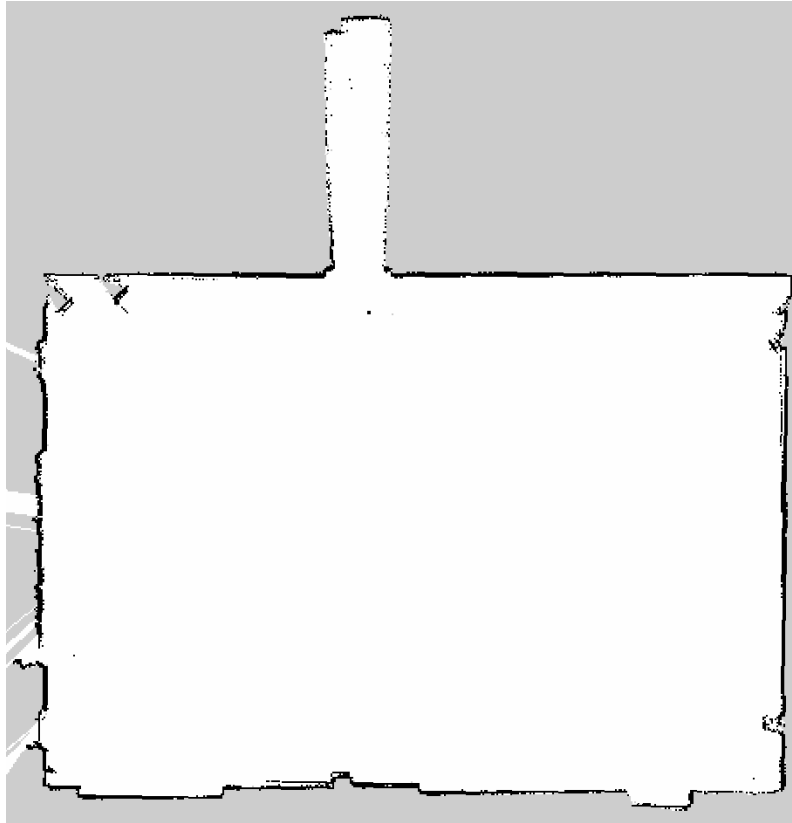


Figure 3. The test environment's map

is limited to 2D. Given that the robot's movement occurs only on a planar surface, we can effectively align and compare the two trajectories.

In order to align the estimated trajectories for subsequent comparison, we adopt a method similar to the approach proposed by Zhang and Scaramuzza [31]. Initially, we synchronize the two trajectories using the global clock provided by ROS. Denoting \mathcal{G}' and \mathcal{P}' , the n ground truth and visual odometry synchronized positions, respectively, defined as follows:

$$\begin{aligned} \mathcal{G}' &= \{\mathbf{g} \mid \|t_{\mathbf{p}} - t_{\mathbf{g}}\| < \tau\} \\ \mathcal{P}' &= \{\mathbf{p} \mid \|t_{\mathbf{p}} - t_{\mathbf{g}}\| < \tau\} \end{aligned} \quad \text{with: } \begin{cases} \forall \mathbf{g} \in \mathcal{G} \\ \forall \mathbf{p} \in \mathcal{P} \\ \tau \in \mathbb{R}^+ \end{cases} \quad (13)$$

Here, $t_{\mathbf{p}}$ and $t_{\mathbf{g}}$ represent the timestamps of points \mathbf{p} and \mathbf{g} , respectively. The synchronization threshold is denoted as τ .

We perform an estimation of the global similarity transformation denoted as \mathbf{S} between the synchronized trajectories of the ground truth (\mathcal{G}') and visual odometry (\mathcal{P}'). This transformation is expressed as $\mathbf{S} = (\mathbf{R}, \mathbf{t}, \lambda)$, where $\mathbf{R} \in \text{SO}(3)$ represents the 3D rotation, $\mathbf{t} \in \mathbb{R}^3$ denotes the translation, and $\lambda \in \mathbb{R}^+$ represents the scale.

The alignment process can be formulated as a least-squares problem, aiming to minimize the discrepancy between the synchronized position pairs $\mathbf{p}_i \in \mathcal{P}'$ and $\mathbf{g}_i \in \mathcal{G}'$. The optimal transformation for global alignment, denoted as $\mathbf{S}^* = (\mathbf{R}^*, \mathbf{t}^*, \lambda^*)$, can be expressed as follows:

$$\mathbf{S}^* = \arg \min_{\mathbf{R}, \mathbf{t}, \lambda} \sum_{i=0}^n \|\mathbf{g}_i - (\lambda \mathbf{R} \mathbf{p}_i + \mathbf{t})\|^2 \quad (14)$$

The estimated visual odometry (VO) trajectory, denoted as \mathcal{P} , is subsequently aligned with the optimal transformation \mathbf{S}^* . This alignment process yields the scaled trajectory \mathcal{P}^* .

$$\forall \mathbf{p} \in \mathcal{P} : \mathcal{P}^* = \{\lambda^* \mathbf{R}^* \mathbf{p} + \mathbf{t}^*\} \quad (15)$$

To assess the performance, we utilize relative errors (REs) as metrics [31]. These REs quantify the disparities between the ground truth and the trajectory generated by Ceiling-DSO. We then calculate the Euclidean norm of the position error to provide an evaluation of the obtained results.

4. Results and discussion

We tested Ceiling-DSO on various sequences extracted from our dataset. For this paper, we have chosen to showcase two specific sequences. The first sequence represents a simple trajectory resembling a square shape, while the second one demonstrates a loop closing trajectory featuring multiple smaller loops.

Initially, we present qualitative results by aligning and visually comparing the aligned trajectories with the corresponding ground truth. Throughout this analysis, we conducted a systematic evaluation by testing a total of 24 trajectories per sequence. These trajectories were generated by iterating over all possible combinations of tested parameters, including two image sizes (848×480 or 424×240), four frame rates (3, 6, 15, or 30fps), and three maximum optimization window sizes (5, 7, or 15). Such testing allows for a systematic examination of the performance of the system across various parameter configurations.

When considering the estimated trajectories from the two sequences, figures 4 and 5 showcase the impact of varying the frame rate and image size while keeping the maximum optimization window size fixed at 7. It is noted that reducing the frame rate below 15fps leads to an increase in trajectory error, which becomes more pronounced in the case of the complex trajectory of the second sequence in figure 5. It is important to highlight that the choice of frame rate is closely linked to the speed of the robot. For robots operating at higher speeds, it becomes necessary to utilize streams with higher frame rates. As DSO implements a coarse-to-fine matching approach, increasing the image size can aid in refining the estimation. However, our tests revealed no significant impact on the estimation accuracy when reducing the image size from 848×480 to 424×240 .

The impact of changing the image size and the maximum optimization window size (while fixing the frame rate at 30fps) on the trajectories can be observed in figures 6 and 7. The trajectories exhibit slight improvements when increasing the maximum window size. This can be attributed to the local bundle adjustment performed during the optimization step. Using a larger window size allows for improved accuracy, particularly in more complex trajectories. However, our tests demonstrated that an acceptable level of accuracy could be achieved with a maximum window size of 7.

For the quantitative analysis, we present the plot of the Euclidean norm of the relative position error $\epsilon_i = \sqrt{\Delta x_i^2 + \Delta y_i^2 + \Delta z_i^2}$ as a function of the traveled distance. Figures 8 and 9 provide a summary of the relative error observed in the two sequences, with each figure representing a variation of one parameter while keeping the other two at their default values (defaults are, image size: 848×420 , frame rate: 30fps, and maximum window size: 7). It is noted from the results that the most significant errors occurred when the frame rate was decreased below 15fps. However, we did not observe any significant influence on the relative error when varying the other parameters.

In order to understand the distribution of relative errors across the entire trajectory and for each parameter combination, we present in figure 10, which provides box plots that depict the relative error distribution, highlighting key statistical measures for each combination of tested parameters. The box represents the *interquartile range (IQR)*, with the first quartile Q_1 and third quartile Q_3 defining its boundaries. The median, denoted as Q_2 , is represented by a line within the box. The whiskers extend from the box to indicate the variability beyond the lower and upper quartiles, within a range of $1.5 \times IQR = 1.5 \times (Q_3 - Q_1)$. This allows for a visual comparison of the relative error distributions for the two sequences.

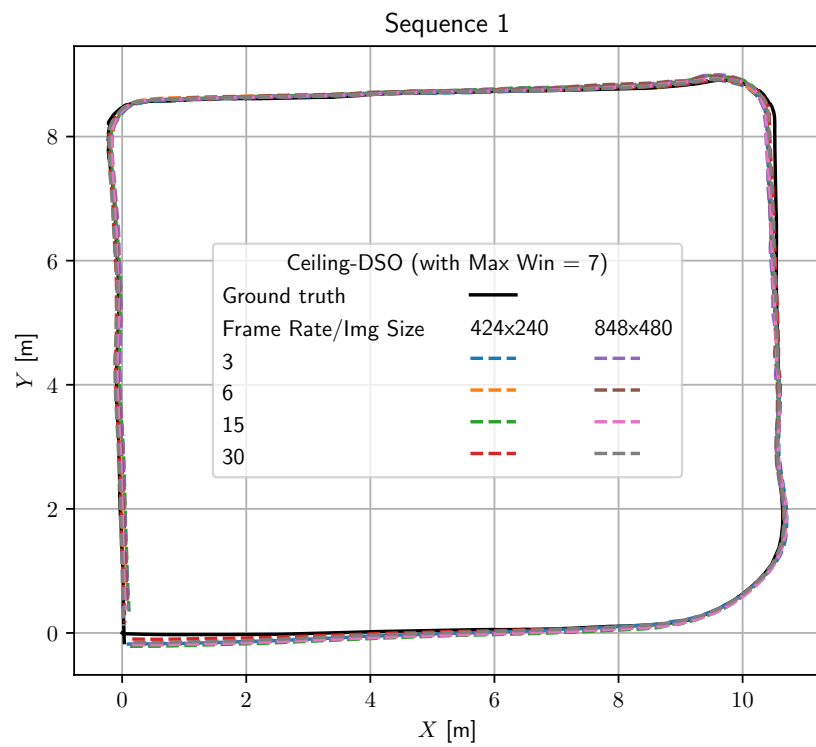


Figure 4. Trajectories for various image sizes and frame rates at a fixed maximum window size of 7 (*sequence 1*).

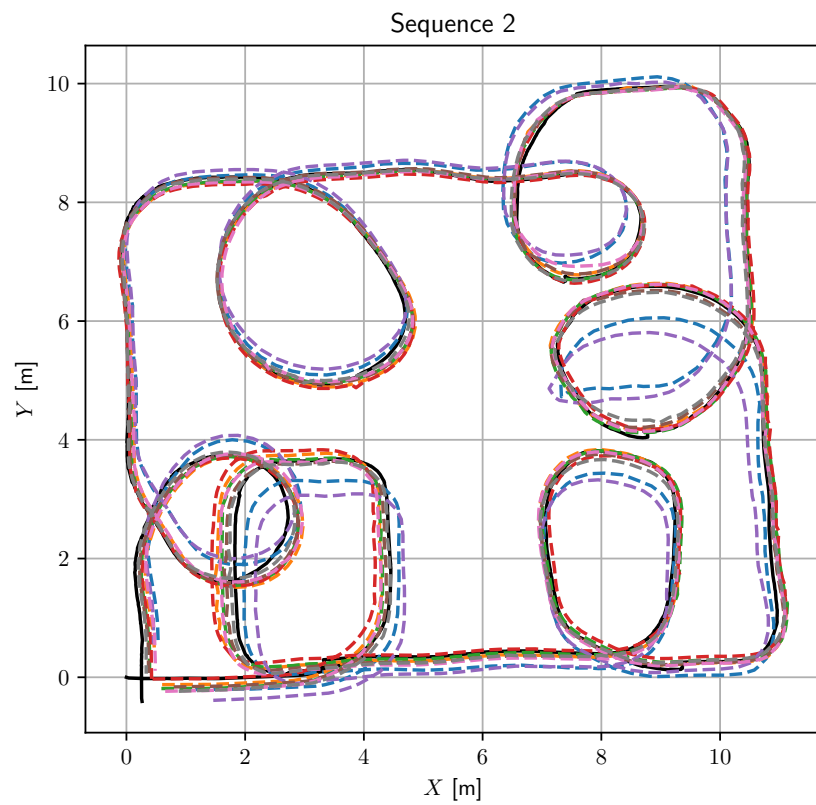


Figure 5. Trajectories for various image sizes and frame rates at a fixed maximum window size of 7 (*sequence 2*).

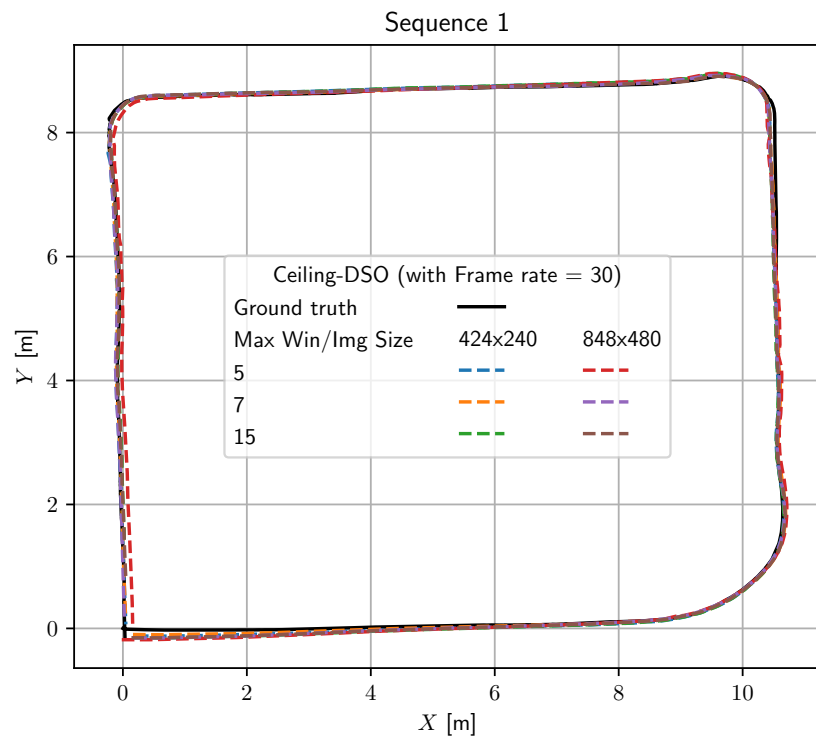


Figure 6. Trajectories for various image sizes and maximum window sizes at a fixed frame rate of 30 (sequence 1).

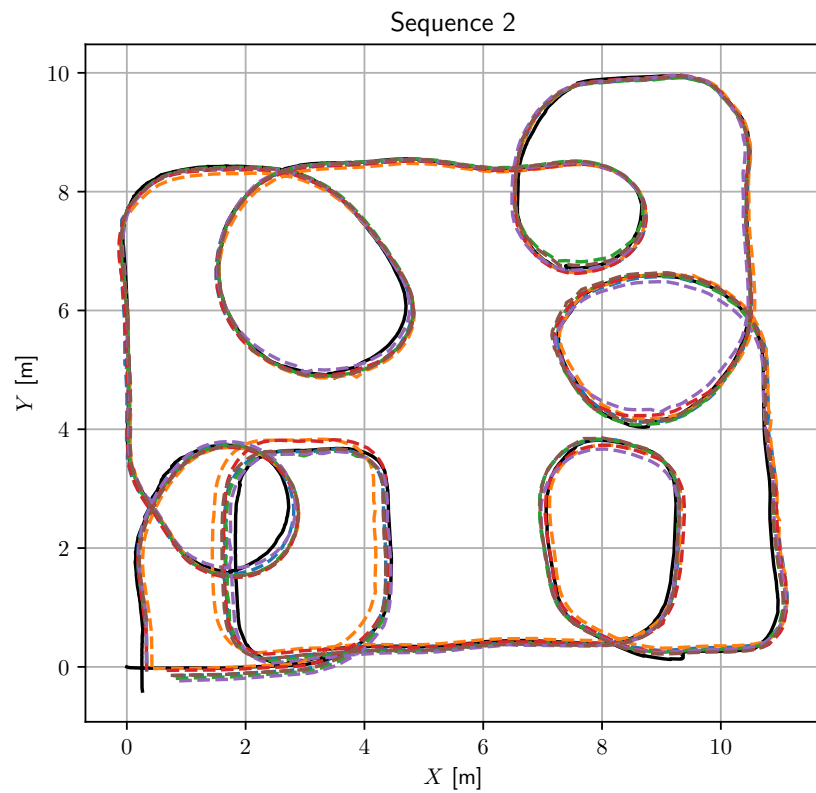


Figure 7. Trajectories for various image sizes and maximum window sizes at a fixed frame rate of 30 (sequence 2).

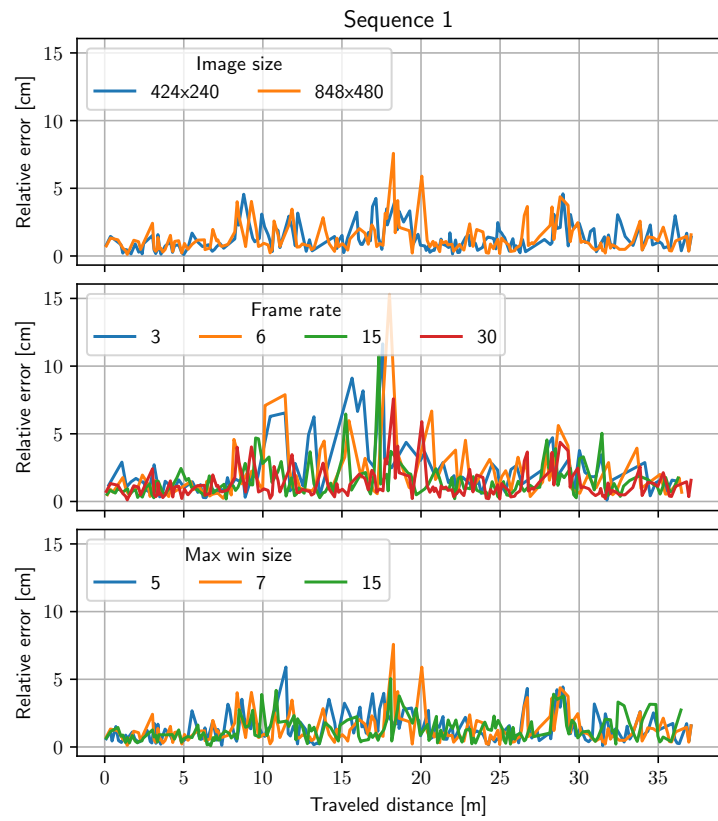


Figure 8. The relative error of the DSO trajectory compared to the ground truth for various frame rates, image sizes, and maximum optimization window sizes (Seq1).

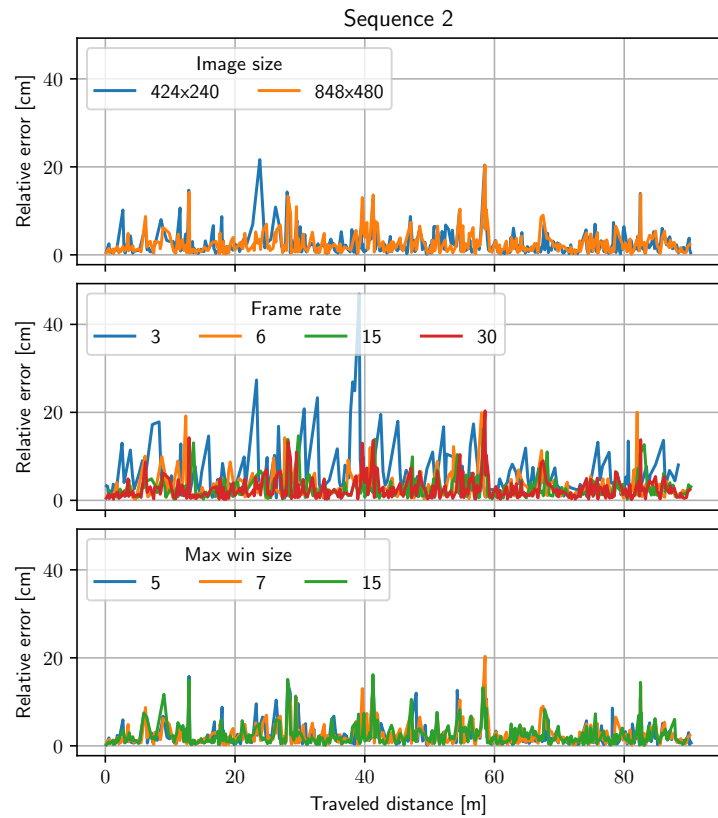


Figure 9. The relative error of the DSO trajectory compared to the ground truth for various frame rates, image sizes, and maximum optimization window sizes (Seq2).

The right subfigure of the plot 10 provides the average execution time per second, which is calculated as the product of the per-frame execution time (t_F) in milliseconds and the frame rate (f) in hertz. These values are obtained from table 1. The vertical green line positioned at $t = 1000\text{ms}$ represents the real-time limit and serves as a reference for determining whether the processing time remains within real-time constraints.

In figure 10, a red dashed line is depicted to bisect the sorted medians of the relative errors. We focus on the parameter combinations in the first half, as they exhibit lower relative errors. Conversely, the second half, which comprises combinations associated with higher relative errors, is mostly characterized by frame rates below 15fps. Notably, the second trajectory demonstrates more pronounced errors. Based on these observations, we can propose a frame rate regulation strategy that aligns with the robot's movement. Specifically, when the robot is moving along a straight line, a lower frame rate can be employed, while an increased frame rate would be preferable during steering maneuvers.

The average execution time per frame was measured for each combination of the tested parameters. The measured timings (in milliseconds) in table 1 provide insights into the *per-frame average execution time*. Surprisingly, reducing the image size did not have a significant impact on the execution time. However, increasing the optimization window size resulted in longer execution times due to the increased workload in each optimization step.

Interestingly, decreasing the frame rate was associated with an increase in the execution time per frame. This counter-intuitive observation can be explained by the fact that the system creates keyframes (which are used in the optimization process) more frequently in low frame rate settings. To support this observation, table 2 presents the ratio of keyframes to frames, revealing no correlation between the window size or image size and the keyframe-to-frame ratio.

Win.	Fps		3	6	15	30
	Image					
5	848 × 480		81.7	50.6	27.5	18.8
	424 × 240		81.8	51.1	27.7	19.2
7	848 × 480		79.6	50.4	27.4	19.2
	424 × 240		79.8	50.0	27.4	19.3
15	848 × 480		200.0	117.0	59.6	38.3
	424 × 240		200.7	117.4	60.1	39.0

Table 1. Average “execution time per frame” (in milliseconds) with respect to the tested parameters

Win.	Fps		3	6	15	30
	Image					
5	848 × 480		0.58	0.35	0.18	0.11
	424 × 240		0.59	0.35	0.18	0.11
7	848 × 480		0.58	0.34	0.18	0.11
	424 × 240		0.58	0.35	0.17	0.11
15	848 × 480		0.61	0.36	0.18	0.12
	424 × 240		0.62	0.36	0.19	0.12

Table 2. Average “keyframe to frame ratio” with respect to the tested parameters

To determine suitable parameters for real-time execution, we calculate the speed factor, which compares the image sampling time to the Ceiling-DSO execution time. The speed factor, denoted as κ , is defined as $\kappa = \frac{1}{t_F \cdot f}$, where t_F represents the per-frame execution time in seconds and f is the frame rate in hertz (both values can be obtained from table 1). A speed factor greater than one ($\kappa > 1$) indicates that the algorithm can process images faster than the frame rate, while a speed factor less than one ($\kappa < 1$) implies that the algorithm

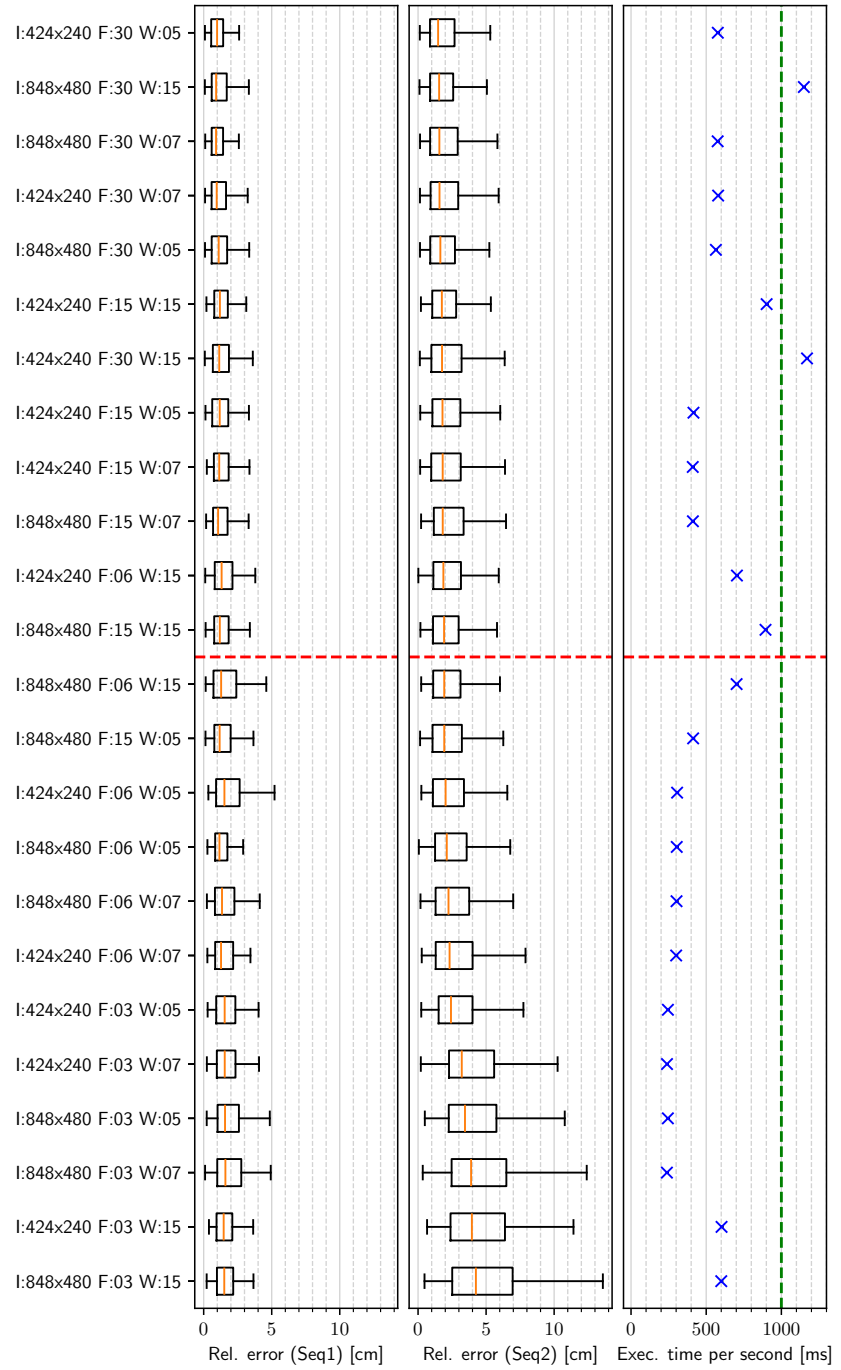


Figure 10. Box plots of relative errors and calculation time for each parameter combination (I: image size, F: frame rate, W: optimization window size). The boxes represent the first and third quartiles, with the orange line indicating the median. Whiskers depict the variability within $1.5 \times \text{IQR}$. Boxes are sorted by Seq2's median relative errors.

cannot process images at the frame rate speed, thereby failing to meet the timing constraints for online processing.

Figure 11 illustrates the speed factor for various combinations of the tested parameters. As indicated in the table 1, there is no apparent correlation between image size and execution time, so the bar plot in the figure marginalizes the influence of image size. The results demonstrate acceptable timing performance, except for the case of a high frame rate of 30fps combined with a maximum window size of 15. From our tests, a window size of 7 appears to offer a good tradeoff between accuracy and runtime.

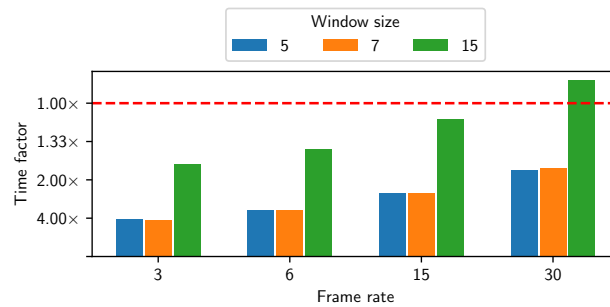


Figure 11. Average *speed factor*. The red dashed line delimits the real-time limit.

5. Conclusions

In this paper, we introduced Ceiling-DSO, an ceiling-vision odometry system based on Direct Sparse Odometry (DSO) specifically designed for applications in indoor mobile industrial robots. One of the key advantages of our system is its suitability for dynamic environments commonly found in industrial settings. Unlike other approaches, our system does not rely on assumptions about the specific shape or content of the ceiling, making it a versatile solution. To validate our approach, we conducted a comparison between the estimated trajectories and the ground truth. Additionally, we conducted experiments to analyze the impact of varying *input image size*, *input frame rate*, and *optimization window size* on the system’s real-time capabilities, with the aim of identifying an optimal parameter combination.

The experimental results indicated that altering the input image size did not have a significant impact on the system’s performance. However, changing the input frame rate had a slight effect on the estimated trajectory and run time. Based on our tests, a frame rate of 15fps offered a good balance between accuracy and run time efficiency. Regarding the optimization window size, varying it did not significantly affect the trajectory accuracy but had a noticeable impact on run time. Our experiments demonstrated that using a maximum window size of 7 provided satisfactory results in terms of both timing and accuracy.

This work serves as a foundation for future research. Our future work will focus on developing an online metric scale estimation approach based on sensor fusion. Additionally, we aim to propose map management and loop-closing strategies to offer a comprehensive SLAM solution for ceiling-vision applications. Furthermore, we plan to make our curated dataset publicly available, enabling other researchers to evaluate and validate their ceiling-vision algorithms using real-world scenarios.

Author Contributions: Conceptualization, A.B., S.B. and E.S.; methodology, A.B. and E.S.; software, A.B.; validation, A.B. and E.S.; formal analysis, A.B.; resources, S.B. and F.G.; data curation, A.B.; writing—original draft preparation, A.B.; writing—review and editing, E.S. and S.B.; visualization, A.B.; supervision, S.B., E.S and F.G.; funding acquisition, S.B, E.S and F.G. All authors have read and agreed to the published version of the manuscript.

Funding: This research received no external funding.

Conflicts of Interest: The authors declare no conflicts of interest.

References

1. Bougouffa, A.; Seignez, E.; Bouaziz, S.; Gardes, F. Evaluation of a Novel DSO-based Indoor Ceiling-Vision Odometry System. In Proceedings of the 2022 17th International Conference on Control, Automation, Robotics and Vision (ICARCV), pp. 47–53. <https://doi.org/10.1109/ICARCV57592.2022.10004272>.
2. Qi, B.; Yang, Q.; Zhou, Y.Y. Application of AGV in Intelligent Logistics System. In Proceedings of the Fifth Asia International Symposium on Mechatronics (AISM 2015), pp. 1–5. <https://doi.org/10.1049/cp.2015.1527>.
3. Borenstein, J. The OmniMate: A Guidewire- and Beacon-Free AGV for Highly Reconfigurable Applications. 38, 1993–2010. <https://doi.org/10.1080/002075400188456>.
4. Han, L.; Qian, H.; Chung, W.K.; Hou, K.W.; Lee, K.H.; Chen, X.; Zhang, G.; Xu, Y. System and Design of a Compact and Heavy-Payload AGV System for Flexible Production Line. In Proceedings of the 2013 IEEE International Conference on Robotics and Biomimetics (ROBIO), pp. 2482–2488. <https://doi.org/10.1109/ROBIO.2013.6739844>.
5. Siegwart, R.; Nourbakhsh, I.R.; Scaramuzza, D. *Introduction to Autonomous Mobile Robots*, 2 ed.; The MIT Press.
6. Scaramuzza, D.; Fraundorfer, F. Visual Odometry [Tutorial]. 18, 80–92. <https://doi.org/10.1109/MRA.2011.943233>.
7. Nister, D.; Naroditsky, O.; Bergen, J. Visual Odometry. In Proceedings of the Proceedings of the 2004 IEEE Computer Society Conference on Computer Vision and Pattern Recognition, 2004. CVPR 2004., Vol. 1, pp. I–I. <https://doi.org/10.1109/CVPR.2004.1315094>.
8. Mur-Artal, R.; Tardós, J.D. ORB-SLAM2: An Open-Source SLAM System for Monocular, Stereo, and RGB-D Cameras. 33, 1255–1262. <https://doi.org/10.1109/TRO.2017.2705103>.
9. Awang Salleh, D.N.S.D.; Seignez, E. Swift Path Planning: Vehicle Localization by Visual Odometry Trajectory Tracking and Mapping. 06, 221–230. <https://doi.org/10.1142/S2301385018500085>.
10. Davison, A.J.; Reid, I.D.; Molton, N.D.; Stasse, O. MonoSLAM: Real-Time Single Camera SLAM. 29, 1052–1067. <https://doi.org/10.1109/TPAMI.2007.1049>.
11. Awang Salleh, D.N.S.D.; Seignez, E. Longitudinal Error Improvement by Visual Odometry Trajectory Trail and Road Segment Matching. 13, 313–322. <https://doi.org/10.1049/iet-its.2018.5272>.
12. Engel, J.; Koltun, V.; Cremers, D. Direct Sparse Odometry. 40, 611–625. <https://doi.org/10.1109/TPAMI.2017.2658577>.
13. Forster, C.; Pizzoli, M.; Scaramuzza, D. SVO: Fast Semi-Direct Monocular Visual Odometry. In Proceedings of the 2014 IEEE International Conference on Robotics and Automation (ICRA), pp. 15–22. <https://doi.org/10.1109/ICRA.2014.6906584>.
14. Geiger, A.; Ziegler, J.; Stiller, C. StereoScan: Dense 3d Reconstruction in Real-Time. In Proceedings of the 2011 IEEE Intelligent Vehicles Symposium (IV), pp. 963–968. <https://doi.org/10.1109/IVS.2011.5940405>.
15. Engel, J.; Schöps, T.; Cremers, D. LSD-SLAM: Large-Scale Direct Monocular SLAM. In Proceedings of the Computer Vision – ECCV 2014; Fleet, D.; Pajdla, T.; Schiele, B.; Tuytelaars, T., Eds. Springer International Publishing, Lecture Notes in Computer Science, pp. 834–849. https://doi.org/10.1007/978-3-319-10605-2_54.
16. Sheng, C.; Pan, S.; Gao, W.; Tan, Y.; Zhao, T. Dynamic-DSO: Direct Sparse Odometry Using Objects Semantic Information for Dynamic Environments. 10, 1467. <https://doi.org/10.3390/app10041467>.
17. Kim, D.H.; Kim, J.H. Effective Background Model-Based RGB-D Dense Visual Odometry in a Dynamic Environment. 32, 1565–1573. <https://doi.org/10.1109/TRO.2016.2609395>.
18. WooYeon, J.; Kyoung, M.L. CV-SLAM: A New Ceiling Vision-Based SLAM Technique. In Proceedings of the 2005 IEEE/RSJ International Conference on Intelligent Robots and Systems, pp. 3195–3200. <https://doi.org/10.1109/IROS.2005.1545443>.
19. Kim, D.Y.; Choi, H.; Lee, H.; Kim, E. A New cvSLAM Exploiting a Partially Known Landmark Association. 27, 1073–1086. <https://doi.org/10.1080/01691864.2013.805470>.
20. Hwang, S.; Song, J. Monocular Vision-Based SLAM in Indoor Environment Using Corner, Lamp, and Door Features From Upward-Looking Camera. 58, 4804–4812. <https://doi.org/10.1109/TIE.2011.2109333>.
21. Choi, H.; Kim, D.Y.; Hwang, J.P.; Park, C.W.; Kim, E. Efficient Simultaneous Localization and Mapping Based on Ceiling-View: Ceiling Boundary Feature Map Approach. 26, 653–671. <https://doi.org/10.1163/156855311X617542>.
22. Choi, H.; Kim, R.; Kim, E. An Efficient Ceiling-view SLAM Using Relational Constraints Between Landmarks. <https://doi.org/10.5772/57225>.
23. Ribacki, A.; Jorge, V.A.M.; Mantelli, M.; Maffei, R.; Prestes, E. Vision-Based Global Localization Using Ceiling Space Density. In Proceedings of the 2018 IEEE International Conference on Robotics and Automation (ICRA), pp. 3502–3507. <https://doi.org/10.1109/ICRA.2018.8460515>.
24. Li, Y.; Zhu, S.; Yu, Y.; Wang, Z. An Improved Graph-Based Visual Localization System for Indoor Mobile Robot Using Newly Designed Markers. 15, 1729881418769191. <https://doi.org/10.1177/1729881418769191>.
25. Schubert, D.; Demmel, N.; Usenko, V.; Stücker, J.; Cremers, D. Direct Sparse Odometry with Rolling Shutter. In Proceedings of the Computer Vision – ECCV 2018; Ferrari, V.; Hebert, M.; Sminchisescu, C.; Weiss, Y., Eds. Springer International Publishing, Lecture Notes in Computer Science, pp. 699–714. https://doi.org/10.1007/978-3-030-01237-3_42.
26. Engel, J.; Usenko, V.; Cremers, D. A Photometrically Calibrated Benchmark For Monocular Visual Odometry, [1607.02555]. <https://doi.org/10.48550/arXiv.1607.02555>.
27. Huber, P.J. Robust Estimation of a Location Parameter. 35, 73–101. <https://doi.org/10.1214/aoms/1177703732>.
28. Solà, J.; Deray, J.; Atchuthan, D. A Micro Lie Theory for State Estimation in Robotics, [1812.01537]. <https://doi.org/10.48550/arXiv.1812.01537>.

29. Bougouffa, A.; Seigneur, E.; Bouaziz, S.; Gardes, F. SmartTrolley: An Experimental Mobile Platform for Indoor Localization in Warehouses. In Proceedings of the 2020 3rd International Conference on Robotics, Control and Automation Engineering (RCAE), pp. 108–115. <https://doi.org/10.1109/RCAE51546.2020.9294484>.
30. Pedrosa, E.; Pereira, A.; Lau, N. Fast Grid SLAM Based on Particle Filter with Scan Matching and Multithreading. In Proceedings of the 2020 IEEE International Conference on Autonomous Robot Systems and Competitions (ICARSC). IEEE, pp. 194–199. <https://doi.org/10.1109/ICARSC49921.2020.9096191>.
31. Zhang, Z.; Scaramuzza, D. A Tutorial on Quantitative Trajectory Evaluation for Visual(-Inertial) Odometry. In Proceedings of the 2018 IEEE/RSJ International Conference on Intelligent Robots and Systems (IROS), pp. 7244–7251. <https://doi.org/10.1109/IROS.2018.8593941>.